Role of surface texture in moisture removal rate and energy efficiency of liquid-desiccant-based air dehumidifiers

Masoud Ahmadi, Behnam Ahmadi, Sajjad Bigham*

Department of Mechanical Engineering-Engineering Mechanics, Michigan Technological University, 1400 Townsend Drive, Houghton, MI, 49931-1295, USA

Abstract

Existing liquid-desiccant-based air dehumidifiers suffer from a poor liquid flow distribution deteriorating moisture removal rate. They are consequently flooded with liquid-desiccant which significantly degrades dehumidification energy efficiency and promotes droplet carryover issues. Here, two novel textured surfaces leveraging engineered wickability effect are introduced to minimize the liquid-desiccant flow required for a fully wetted dehumidifier surface. This subsequently improves both moisture removal rate and dehumidification energy efficiency. The new textured surfaces rely on tuned capillary forces eliminating the desiccant droplet carryover issue under high air velocities. A systematic flow visualization study showed that the texture length scale is optimized at an intermediate texture density. Dry patches appear at length scales exceeding the optimum texture distance while the effective liquid-air interfacial area is reduced at smaller length scales, both of which decrease the moisture removal rate. At the optimum texture density, the effective liquid-air interfacial area of each textured surface increases with the solution flow rate, thereby improving the dehumidification rate. At a water vapor pressure potential of 2.3 kPa and a solution flow rate of 2.8 g/s, experimental results indicated a moisture removal rate of 0.1 g/m^2-s for the proposed textured dehumidifier surface, a 37% improvement compared with that of advanced internally-cooled membrane-based liquid-desiccant dehumidifiers. A high moisture removal rate of the textured surface at a low desiccant flow rate led to an overall system thermal efficiency of 0.75, a 53% enhancement compared with the membrane-based liquid-desiccant dehumidifiers. The insights gained from the present study guide design of advanced textured surfaces for next-generation high-performance liquid-desiccant-based air dehumidification systems.

Keywords: Air dehumidification; Textured surfaces; Moisture removal rate; Energy efficiency; Wickability

Nomenclatures

AC	Air conditioning	*Symbols*	
VCR	Vapor compression refrigeration	v	Velocity
SSLC	Separate sensible and latent cooling	T	Temperature
Greek letters		x	Desiccant concentration
Γ	Flow rate per length	p	Pressure
η	Effectiveness	J	Dehumidification rate

*Corresponding author. Tel.: +1 906 487 2747.
Email address: sbigham@mtu.edu (S. Bigham)

ρ	Density	h_{fg}	Latent heat of vaporization
Chemical symbols		$P_{wv,air}$	Partial water vapor pressure of the air side
LiBr	Lithium Bromide	$P_{wv,LiBr}$	Partial water vapor pressure of the LiBr solution
$H2O(v)$	Water vapor	*Subscripts*	
$H2O(l)$	Liquid water	Sol.	Solution
		In/Out	Inlet/Outlet

1. Introduction

The International Energy Agency (IEA) predicts that the air conditioning (AC) systems will emerge as the second-largest driver of global electricity demand after the industry sector over the next three decades [1]. Although providing substantial benefits in increased human health and comfort for billions of people, the fast-rising AC demand particularly in the emerging world introduces significant energy challenges combined with massive climate risks. Particularly, an extensive additional power generation capacity is needed to meet the power requirements of these new AC systems. Furthermore, current AC systems cool our buildings at the expense of warming the planet. It is estimated that the growing AC demand would alone add 0.4-0.8°C to global warming by 2050 [1]. This is a striking number considering that the total global average temperature rise in the current century targeted by the Paris Climate Agreement is well below 2°C above pre-industrial levels.

One plausible pathway to address the above energy and climate concerns is to invest in advanced energy-efficient AC solutions including separate sensible and latent cooling (SSLC) systems. Existing vapor-compression-based AC systems cannot independently manage building sensible and latent cooling loads. This results in substantial overcooling of the supply air to below its dew point combined with a potential heating process, both of which reduce the energy efficiency of standard AC systems. The SSLC systems, on the other hand, employ a dedicated moisture management unit to separately treat building latent load (i.e., humidity), thereby boosting AC energy performance [2]. Particularly, the liquid-desiccant-based air dehumidifiers are deemed a promising environmentally-friendly solution to curtail energy consumption of AC systems [3,4].

The architectural design of a liquid-desiccant-based air dehumidifier plays a significant role in both moisture removal rate (i.e., size and capital cost) and overall energy efficiency (i.e., operating cost) of the dehumidifier module. A poorly designed dehumidifier module results in a bulkier, costlier, and less energy-efficient AC system. Packed bed air dehumidifiers provide a substantial desiccant-air interfacial area and are currently the dominant liquid-desiccant-based dehumidifier architecture [5–13]. Naik et al. [14] experimentally investigated performance of a packed bed dehumidifier. It was found that dehumidification performance of the packed chamber dehumidifier strongly depends on liquid-desiccant enthalpy and air humidity ratio. They also observed a drop in dehumidification rate when the liquid-to-air flowrate ratio increases. Cho et al. [15] compared dehumidification performance of a CELdek packed tower liquid-desiccant dehumidifier in cross- and counter-flow directions. Their experimental data showed that the counter-flow configuration has a 19% higher dehumidification effectiveness than that of the cross-flow packed tower dehumidifier at high inlet air velocities. However, they reported a higher possibility of the droplet carryover issue in a counter-flow dehumidifier. Considering manufacturability, cost, and maintenance problems of the commercially available CELdek packed media, Salins et al. [9] recently proposed wood shaving packed media for liquid-desiccant dehumidifiers. They fabricated a liquid-desiccant dehumidifier made of organic biomass packed media a density of 500 kg/m^3. They found that dehumidification performance of the wood shaving is slightly inferior to that of the CELdek packing. However, packed bed liquid-desiccant air dehumidifiers introduce a substantial air-side pressure drop and demonstrate the desiccant droplet carryover issue.

Plate-type liquid-desiccant air dehumidifiers are deemed a promising solution to address the high air-side pressure drop penalty associated with the packed bed liquid-desiccant dehumidifiers. The liquid-desiccant flow mal-distribution, however, has been identified as one of the major barriers withholding the wide commercial usage of the plate-type liquid-desiccant dehumidifier systems [16]. A thick, non-uniform solution film deteriorates the performance of a plate-type dehumidifier module in four different ways. First, a thick desiccant solution film introduces a high thermal resistance to cool the desiccant-air interface, thereby reducing the moisture removal rate. Second, a thick solution film results in a high solution flow rate. At higher solution flow rates, the thermal energy required for the desorption process is higher, thereby decreasing overall energy efficiency. Third, a thick solution film is more susceptible to the desiccant droplet carry-over issue [17,18]. Forth, a non-uniform solution film leads to dry areas with little-to-no dehumidification rates. Therefore, achieving a thin and uniform liquid-desiccant flow distribution over solid surfaces of a plate-type dehumidifier module is the key factor affecting dehumidification performance.

Prior studies have examined coated surfaces through chemical/physical methods [19–24] and/or surfactant [25,26] or nanoparticles [27–29] added to the solution to improve the liquid-desiccant flow distribution over solid surfaces of an air dehumidifier. These methods promote surface wettability by reducing the liquid-desiccant contact angle, thereby better distributing the liquid-desiccant solution. Dong et al. [24] successfully decreased the stainless-steel surface free energy and lowered the contact angle of deionized water from 90° to 10°. The dehumidification rate was then improved by as high as 60%. Their dynamic modeling also showed more than 9% of electricity saving could be achieved by using a TiO2 coating. In another study, Wen et al. [25] investigated the dehumidification performance of the LiCl solution in the presence of the PVP K-30 additive. They showed the additive improves the wetting properties of the surface, which resulted in a 22.7% enhancement in the dehumidification rate. Although the above approaches improve wettability and dehumidification rate, they lose their functionality with time and thus require periodic retreatment of the dehumidifier surface. Additionally, these methods often reduce the liquid-desiccant contact angle (i.e., weaken the capillary and adhesion forces), thereby stimulating the desiccant droplet carry-over issue.

Alternatively, membrane-based liquid-desiccant air dehumidifiers are proposed to improve solution flow distribution and mitigate the desiccant droplet carry-over issue [30–39]. In a membrane-based dehumidifier, the liquid-desiccant is constrained between a solid wall and a vapor-permeable superhydrophobic membrane, thereby allowing a uniform liquid-desiccant flow distribution. Here, the membrane barrier only allows water vapor molecules to pass through the membrane, and thus suppresses the droplet carryover issue. Woods and Kozubal [37] proposed a membrane-based air dehumidifier called a desiccant-enhanced evaporative (DEVap) air conditioner to mitigate the desiccant droplet carryover and associated corrosion issues. The liquid-desiccant flow was cooled through an indirect evaporating water film which resulted in a 0.053 g/m^2-s dehumidification rate. Xiao et al. [31] evaluated dehumidification characteristics of an internally-cooled membrane-based liquid-desiccant dehumidifier. They studied effects of main operating parameters including air temperature, relative humidity, and velocity on system performance. The results showed a high dehumidification rate of 0.073 g/m^2-s with a coefficient of performance in the range of 0.46-0.62. The thermal energy consumption of the regeneration process was above 60% of the total energy input. However, the membrane barrier introduces an additional mass resistance to the water vapor transport process, thereby potentially reducing the dehumidification rate. Furthermore, membranes are susceptible to scaling/fouling and deflection issues, and thus demonstrate a low longevity [36].

In this study, two novel textured surfaces leveraging wickability effect are introduced to (i) minimize the liquid-desiccant flow required for a fully wetted dehumidifier surface, and (ii) mitigate the desiccant droplet carryover issue. Although textured surfaces have been examined for closed vacuum-proof absorption systems [19,40–42], they are not considered for open atmospheric air dehumidifier systems mainly due to the droplet carryover issue. Particularly, open liquid-desiccant dehumidification systems experience high air velocities (i.e., high shear forces) at the desiccant-air interface with a high possibility of the droplet carryover issue. However, the wickability effect and capillary forces of a textured surface can be engineered to both uniformly distribute the desiccant solution and overcome the droplet carryover issue. Here, interfacial flow physics and dehumidification performance of the two textured surfaces with drop-shaped structures and partitioned offset-strip fins are extensively examined. In the following sections, first, the intertwined dependency between different parameters of the liquid-desiccant-based air dehumidification process on textured surfaces is explained. Next, the design and development of the textured dehumidifier module and dehumidification test facility are discussed. Finally, the moisture removal rate and energy performance of the liquid-desiccant-based air dehumidifier on textured surfaces at different thermo-hydraulic operating conditions are examined.

2. Concept

In this study, polymeric textured surfaces are examined to improve the moisture removal rate and energy efficiency of liquid-desiccant-based air dehumidifier systems. In contrast to metals, polymers do not suffer from corrosion issues posed by a liquid desiccant [43]. However, surfaces made of polymers demonstrate low surface energy in which the contact angle between a liquid desiccant (e.g., lithium bromide) and the polymer surface is intrinsically high [16,44–46]. Under this condition, the design of such a low-surface-energy surface should mostly rely on wickability rather than the wettability effect. However, there is a complex dependency between the length scale of a surface structure, desiccant flow rate, liquid contact angle, liquid-air interfacial area, and air dehumidification rate. The two extreme conditions for a textured surface are a plain surface (i.e., no texture) and a highly dense texture pattern. The liquid-desiccant flow distribution on a plain surface results in discrete rivulets with a limited dehumidification rate. A surface with a highly dense texture pattern poses a high solid fraction area, and thus a limited effective liquid-air interfacial area and dehumidification rate. Therefore, there is an intermediate texture density at which the dehumidification rate maximizes.

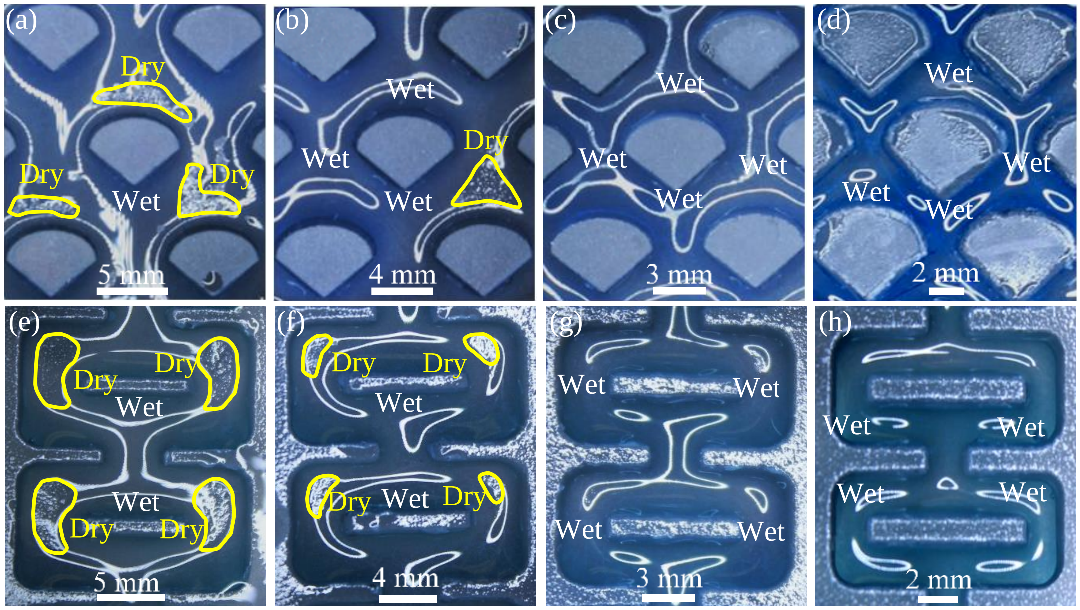

Fig. 1: Liquid flow distribution patterns for textured surfaces with drop-shaped (a-d) and partitioned offset-strip fin (e-h) structures at different texture spacing. The closed regions highlighted in yellow indicate dry patches (i.e., solid-air interfacial area) with minimum-to-no dehumidification rate.

In this study, two types of textured surfaces with drop-shaped structures (cf. Fig. 1a-d) and partitioned offset-strip fins (cf. Fig. 1e-h) were studied. To determine the optimum texture density of each surface, four different edge-to-edge structure spacing of 5, 4, 3, and 2 mm were examined. Each textured surface was fabricated on a polycarbonate sheet. The liquid flow distribution pattern of each textured surface was examined at a nominal flow rate per length of Γ=12.65 g/m-s. Fig. 1 shows the liquid flow distribution patterns of the examined textured surfaces. The closed regions highlighted in yellow indicate dry patches (i.e., solid-air interfacial area) with a little-to-no dehumidification rate. As evident, in both texture types, dry patches appear when the texture length scale (i.e., edge-to-edge texture spacing) is 4 mm or larger. As the texture length scale decreases, dry areas shrink in size due to an augmented wickability effect. At a texture length scale of 3 mm, capillary forces of both texture types promote a strong wickability effect, thereby resulting in a fully wetted condition. Although the capillary forces become stronger at texture length scales smaller than 3 mm, the effective liquid-air interfacial area negatively decreases. As shown in Fig. 2, the percentage liquid-air interfacial area

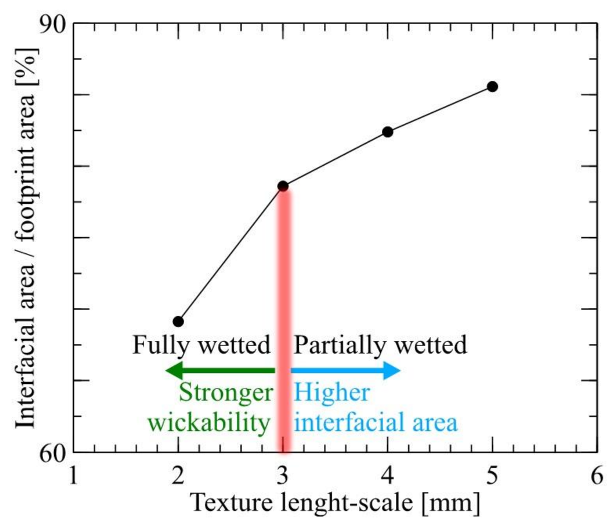

Fig. 2: Percentage liquid-air interfacial area available for the dehumidification process versus texture length scale for the partitioned offset-strip fin structure.

available for the dehumidification process decreases at smaller texture length scales. For instance, the available liquid-air interfacial area shrinks from 79% to 69% when the texture length scale decreases from 3 to 2 mm, respectively. Therefore, a texture length scale of 3 mm for both textured surfaces employing the drop-shaped structures and partitioned offset-strip fins was chosen. Fig. 3 shows images of the two textured surfaces that were evaluated for the dehumidification tests. Both textured surfaces were made of polycarbonate with dimensions of 18" × 12" × 0.375".

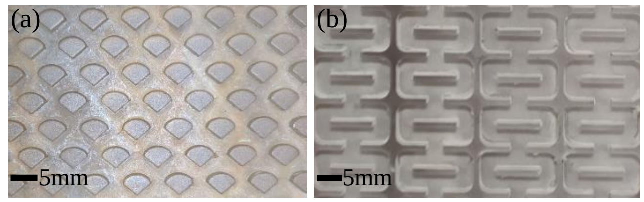

Fig. 3: Images of textured surfaces with (a) drop-shaped structures, and (b) partitioned offset-strip fins. The texture length scale of both surfaces is 3 mm.

3. Experiment and uncertainty analysis

3.1. Textured dehumidifier module

Fig. 4 shows a textured dehumidifier module fabricated to examine the dehumidification performance of the two textured surfaces discussed in the previous section. The dehumidifier module consists of a dehumidifier surface with either drop-shaped textures or partitioned offset-strip fins, a brass liquid-desiccant solution distributor, two transparent cover plates, two 3D-printed air manifolds, and two probe holders. The liquid-desiccant solution of the present study is lithium bromide (LiBr). The solution distributor unit uniformly distributes the LiBr solution over the dehumidifier textured surface. The LiBr solution then flows downward due to gravity. A humid air stream, flowing from left to right, gets in contact with the LiBr solution and is thus dehumidified. As shown in the inset image of Fig. 4b, the probe holder installed at the inlet and outlet ports hosts five thermocouples and one humidity sensor, thereby providing an average air temperature of the cross-section. The performance of the dehumidifier module is evaluated in a dehumidification test facility as discussed below.

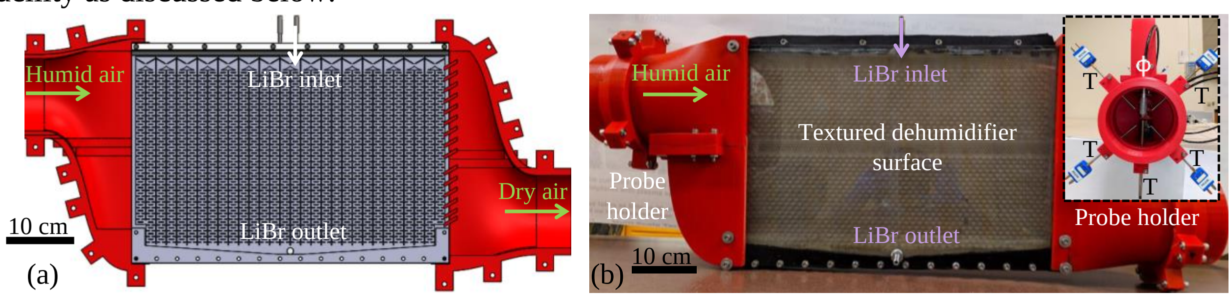

Fig. 4: (a) A cross-sectional view, and (b) an actual image of the dehumidifier module. The inset image shows a zoomed view of a probe holder with five embedded thermocouples and one embedded humidity sensor.

3.2. Dehumidification test facility

Fig. 5 shows a schematic and an image of the experimental test facility to evaluate dehumidification performance. The dehumidification test facility has two main flow loops: the liquid-desiccant and air flow loops. The test facility is well equipped to fully monitor, control, and measure important thermo-hydraulic properties of the liquid-desiccant and air flow streams. This allows to comprehensively evaluate heat and mass transfer performance of the dehumidifier module under a wide range of working conditions. Details of each flow loop are discussed in the following sections.

Liquid-desiccant flow loop: As shown in Fig. 5, the liquid-desiccant flow loop consists of the dehumidifier module, a desorber module, a solution heat exchanger unit, two solution pumps, and two Coriolis mass flow meters. The two Coriolis flowmeters (Model: Emerson Electric Co., Micro Motion Elite Coriolis Flow/Density Meter, CMFS series) measure the LiBr mass flow rate, temperature, and density before and after the dehumidifier module. A strong LiBr solution flows through the dehumidifier module. Here, the strong LiBr solution, exposed to the humid air stream, captures the airborne moisture and becomes weak in concentration. The weak LiBr solution is then pumped to the desorber module. In the desorber module, a hot oil stream supplying thermal energy to the desiccant solution desorbs the captured humidity and regenerates the strong LiBr solution. A solution heat exchanger is positioned between the desorber and dehumidifier modules to transfer heat from the high-temperature LiBr solution leaving the desorber module to the low-temperature LiBr solution exiting the dehumidifier module. Therefore, the solution heat exchanger reduces the input thermal energy of the desorber module. The strong LiBr solution leaving the desorber then flows back to the dehumidifier module to complete the LiBr flow loop.

Air flow loop: The air flow loop consists of a mist generator, an air heater/cooler unit, a circulating fan, an air flow meter, and several thermocouples (Model: ReoTemp F-M12T1SU4) and humidity measurement station points. A honeycomb laminated air flow meter (Model: Air Monitor Inc., 4" LO-flo/P with an integral temperature probe) provides highly accurate measurements of the air volumetric flow rate in the range of 0 to 400 CFM. Three warmed-probe humidity sensors (Model: Vaisala Inc., HMT 337) provide fast and reliable humidity measurements at low to highly humid conditions. They are positioned at the inlet and outlet of the dehumidifier module and the outlet of the desorber module. The air flow loop interacts with the desiccant flow loop through the dehumidifier module. The loop can generate a target warm and humid air stream at the inlet of the

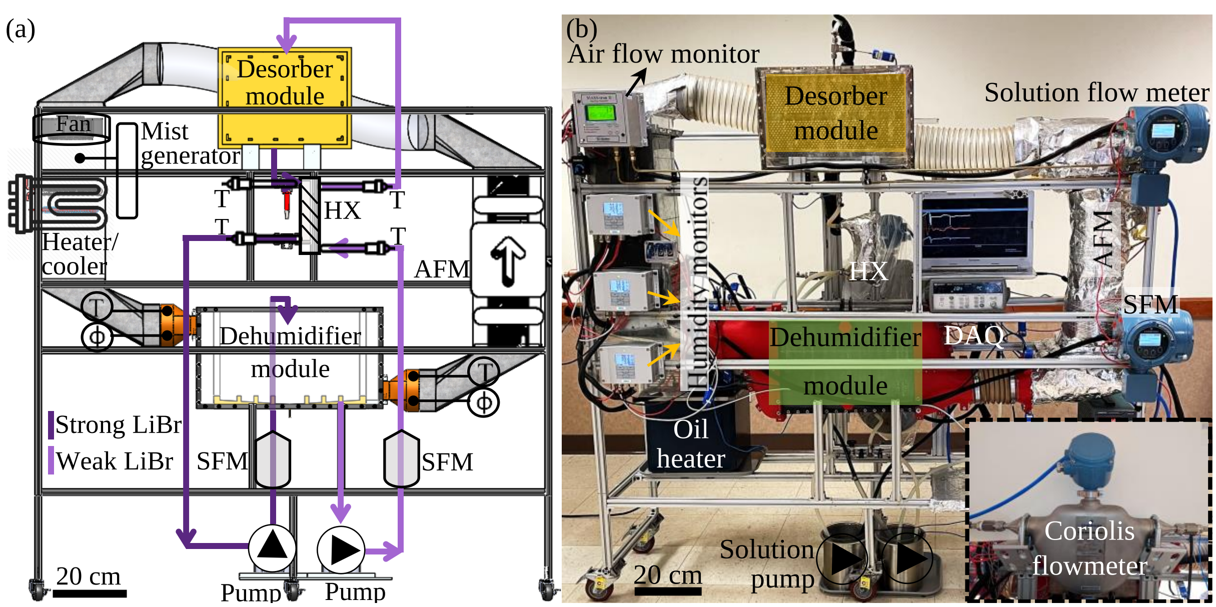

Fig. 5: (a) A schematic, and (b) an image of the dehumidification test facility. AFM, SFM, HX, and DAQ stand for air flow meter, solution flow meter, heat exchanger, and data acquisition, respectively.

dehumidifier module. The warm and moist air stream then enters the dehumidifier (i.e., absorber) module. Here, the air moisture is absorbed by the LiBr solution. The heat released during the absorption process is partially transferred to the air stream. During the dehumidification tests, the temperature and humidity of the air at the inlet and outlet of the dehumidifier module are closely monitored.

3.3. Data reduction and uncertainty analysis

Table 1 lists nominal value, range, experimental error, and uncertainty of main experimental parameters including solution flow rate, solution density, solution temperature, air flow rate, air temperature, and relative humidity. The dehumidification rate (J_{deh}) is defined as the net moisture removal rate per projected area as follows:

$$J_{deh} = \frac{\dot{m}_{LiBr}(x_{in,deh} - x_{out,deh}) - \dot{m}_{cond}}{A_{proj}}, \; x_{LiBr} = f(T_{LiBr}, \rho_{LiBr}) \tag{1}$$

where $\dot{m}_{LiBr}$ is the LiBr solution flow rate, x is the LiBr concentration which is a function of LiBr temperature (T_{LiBr}) and density (ρ_{LiBr}), $\dot{m}_{cond}$ is condensation rate on the cover sheets, and A_{proj} is the projected area for the absorption process. A series of dedicated experiments were conducted to determine the condensation rate of the cover sheets under different air temperature, humidity, and velocity conditions. In these tests, the LiBr solution flow rate of the dehumidifier module was zero.

The uncertainty associated with the dehumidification rate is calculated as follows:

$$\frac{\delta J_{deh}}{J_{deh}} = \sqrt{\left(\frac{\delta \dot{m}_{LiBr}}{\dot{m}_{LiBr}}\right)^2 + 2\left(\frac{\delta \rho_{LiBr}}{\rho_{LiBr}}\right)^2 + 2\left(\frac{\delta T_{LiBr}}{T_{LiBr}}\right)^2 + \left(\frac{\delta \dot{m}_{cond}}{\dot{m}_{cond}}\right)^2} \tag{2}$$

The performance of the dehumidifier module is a strong function of the water vapor pressure difference in the air and LiBr solution sides. The water vapor pressure potential is calculated as follows:

$$\Delta P = P_{wv,air,inlet}(T_{air}, \phi_{air}) - P_{wv,LiBr,inlet}(T_{LiBr}, x_{LiBr}) \tag{3}$$

where $P_{wv,air}$, the partial water vapor pressure of the air, is a function of air temperature (T_{air}) and humidity (ϕ_{air}), and $P_{wv,LiBr}$ is the partial water vapor pressure of the LiBr solution.

The overall system thermal efficiency for the dehumidification process is also defined as follows:

$$\varepsilon = \frac{\dot{m}_{air}(\omega_{air,out} - \omega_{air,in})h_{fg}}{\dot{Q}_{net,desorber}} \tag{4}$$

where $\dot{m}_{air}$ is the air flow rate, ω_{air} is the air humidity ratio, h_{fg} is the water latent heat of evaporation, and $\dot{Q}_{net,desorber}$ is the net input thermal energy of the desorber module. The uncertainty associated with the system energy efficiency is calculated as follows:

$$\frac{\delta\varepsilon}{\varepsilon} = \sqrt{\left(\frac{\delta \dot{m}_{air}}{\dot{m}_{air}}\right)^2 + \left(\frac{\delta \omega_{air,in}}{\omega_{air,in}}\right)^2 + \left(\frac{\delta \omega_{air,out}}{\omega_{air,out}}\right)^2 + \left(\frac{\delta \dot{Q}_{net,desorber}}{\dot{Q}_{net,desorber}}\right)^2} \tag{5}$$

where

$$\frac{\delta \dot{Q}_{net,desorber}}{\dot{Q}_{net,desorber}} = \sqrt{\left(\frac{\delta \dot{m}_{LiBr}}{\dot{m}_{LiBr}}\right)^2 + 2\left(\frac{\delta T_{LiBr}}{T_{LiBr}}\right)^2 + \left(\frac{\delta \dot{m}_{v}}{\dot{m}_{v}}\right)^2} \tag{6}$$

where $\dot{m}_v$ is the vapor generation rate defined as follows:

$$\dot{m}_v = \dot{m}_{LiBr}(x_{out,des} - x_{in,des}) \tag{7}$$

In addition, the uncertainty associated with the vapor generation rate is calculated as follows:

$$\frac{\delta \dot{m}_v}{\dot{m}_v} = \sqrt{\left(\frac{\delta \dot{m}_{LiBr}}{\dot{m}_{LiBr}}\right)^2 + 2\left(\frac{\delta T_{LiBr}}{T_{LiBr}}\right)^2 + 2\left(\frac{\delta \rho_{LiBr}}{\rho_{LiBr}}\right)^2} \quad (8)$$

Table 1: Nominal value, range, experimental error, and uncertainty of main parameters.

Parameter [unit]	**Nominal value**	**Range**	**Experimental error**	**Uncertainty**
LiBr solution flow rate [g/s]	3.1	1.6 - 4.6	± 0.31	± 0.1 %
LiBr solution density [kg/m^3]	1483	1480 - 1485	± 0.5	± 0.03 %
LiBr solution temperature [°C]	30	25 – 35	± 1	± 0.33 %
Air flow rate [CFM]	20	0 - 40	± 0.4 %	± 2 %
Air relative humidity [%]	80	40 - 90	± 0.11	± 1.7 %
Air temperature [°C]	45	40 - 85	± 0.2	± 0.33 %

3.4. Test procedure

The test procedure followed for each experimental data point presented in the result section is described in detail here. The first step was to adjust the air blower speed to deliver a target air flow rate. Next, a desired air flow temperature/humidity condition at the inlet of the dehumidifier module was set. This was accomplished by simultaneous adjustment of a mist generation unit, an electric heater, and a chilled heat exchanger unit. Then, target solution flow rates for the dehumidifier and desorber modules were set. The final step was to adjust the hot oil temperature providing thermal energy to the desorber module.

The following parameters were continuously monitored during each test to ensure a steady-state operation: air flow rate, dehumidifier inlet air temperature, dehumidifier inlet air relative humidity, dehumidifier/desorber inlet/outlet LiBr concentration, and dehumidifier/desorber inlet/outlet LiBr temperature/density. Each experimental test was allowed for at least 30 minutes to reach a steady-state condition at which there was no continuous rise and/or decline in the mentioned parameters. Additionally, each test was repeated at least three times to ensure repeatability of the data presented.

4. Results and discussion

The test facility described in the previous section was employed to evaluate the performance of the two textured dehumidifier surfaces over a wide range of climate conditions. During the dehumidification tests, the partial water vapor pressure of the inlet LiBr solution was kept constant as the inlet LiBr temperature and concentration of the dehumidifier module were kept fixed at 30°C and 47%, respectively. Therefore, different partial water vapor potentials were established by varying the inlet air conditions of the dehumidifier module.

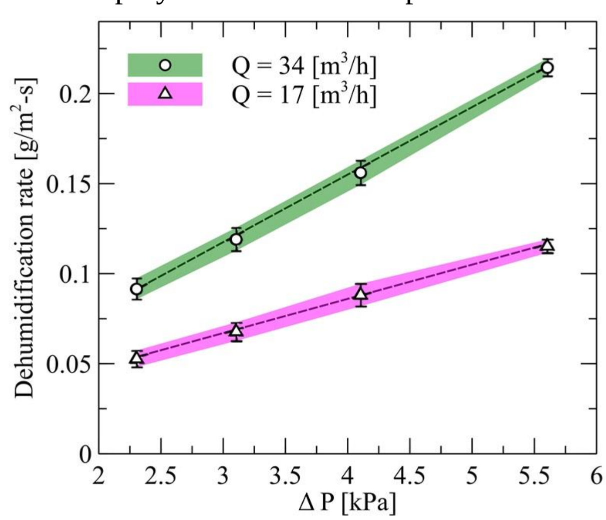

Fig. 6: Dehumidification rate of the textured surface with the drop-shaped structures as a function of the water vapor pressure potential at two different air flow rates.

4.1. Role of air flow rate in the dehumidification process

Fig. 6 shows the dehumidification rate of the textured surface with drop-shaped structures as a function of the water vapor pressure potential at two different air flow rates of 17 and 34 m^3/h. The LiBr flow rate is kept constant at 2.8 g/s. The corresponding air temperature/humidity and LiBr temperature/concentration conditions are listed in Table 2. As evident, the dehumidification rate linearly increases with the water vapor pressure potential at both air flow rates. Additionally, the dehumidification rate increases at higher air flow rates. For instance, the dehumidification rate increases by 86% when the air flow rate doubles at a water vapor pressure potential of 5.6 kPa. This is attributed to the moisture boundary layer thickness at the desiccant-air interface, which shrinks at higher air flow velocities. A thinner moisture boundary later introduces a lower resistance to the mass transfer process of the water vapor molecules, thereby increasing the dehumidification rate.

Table 2: LiBr and air operating conditions for the dehumidification tests at two different air flow rates.

LiBr operating conditions			**Air operating conditions**			**Dehumidification rate [g/m^2-s]**	
$T_{LiBr,in}$ [°C]	$X_{LiBr,in}$ [%]	$P_{wv,LiBr,in}$ [kPa]	$T_{air,in}$ [°C]	$\Phi_{air,in}$ [%]	$P_{wv,air,in}$ [kPa]	Q_{air} = 17 [m^3/h]	Q_{air} = 34 [m^3/h]
30	47	1.48	34	70	3.78	0.053	0.092
			36	77	4.58	0.068	0.12
			37	85	5.58	0.088	0.16
			39	99	7.08	0.115	0.214

4.2. Role of surface texture in the dehumidification process

Fig. 7 shows the dehumidification rate of the textured surfaces employing the drop-shaped structures (i.e., 1st gen.) and partitioned offset-strip fins (i.e., 2nd gen.) as a function of the water vapor pressure potential. The air flow rate is kept constant at 34 m^3/h. As evident, the dehumidification rate of both textured surfaces linearly increases with the water vapor pressure potential. However, the textured surface utilizing the partitioned offset-strip fins outperforms the textured surface with the drop-shaped structures in all LiBr solution flow rates. The advantage of the second-gen. textured surface design is particularly more pronounced at higher solution flow rates. For instance, at a LiBr solution flow rate of 4.1 g/s and a partial water vapor potential of 5.6 kPa, the dehumidification rate of the partitioned offset-strip fins is 33% higher than that of the drop-shaped structures. This indicates that the partitioned offset-strip fins offer a better LiBr flow distribution with an augmented desiccant-air interfacial area compared with the drop-shaped structures.

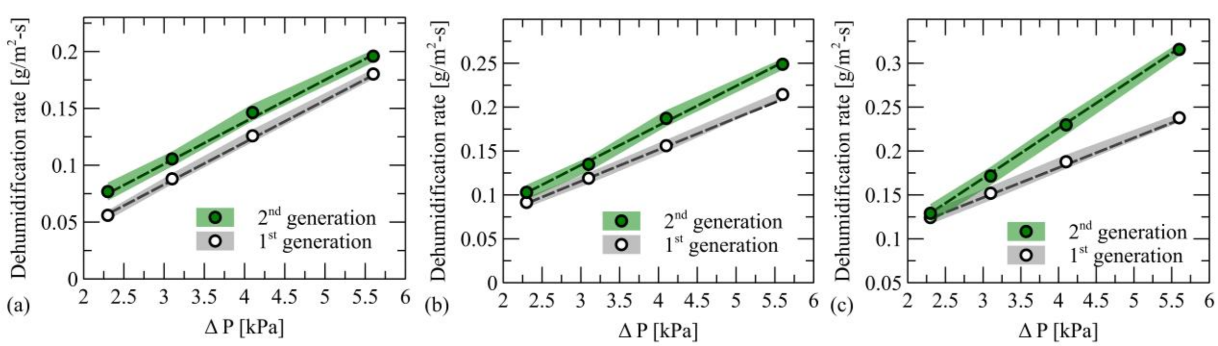

Fig. 7: Dehumidification rate of the textured surfaces with the drop-shaped structures (i.e., 1st gen.) and partitioned offset-strip fins (i.e., 2nd gen.) as a function of the water vapor pressure potential at three different LiBr solution flow rates of (a) 1.6, (b) 2.8, and (c) 4.1 g/s.

4.3. Role of LiBr solution flow rate in the dehumidification process

Fig. 8 shows the dehumidification rate of the textured surface with the partitioned offset-strip fins versus the water vapor pressure potential at three different LiBr solution flow rates of 1.6, 2.8, and 4.1 g/s. At a fixed water vapor pressure potential, the dehumidification rate increases with the LiBr solution flow rate. This is attributed to the desiccant-air interfacial area, which increases with solution flow rate. This effect is highlighted in Fig. 9 showing interfacial flow patterns of the 2nd generation texture design at different solution flow rates of 1.6, 2.8, 4.1, 5.4, and 6.5 g/s. As evident, at a solution flow rate of 1.6 g/s, the dry areas (i.e., solid-air menisci) cover a significant portion of the surface. The dry areas do not effectively participate in the dehumidification process. As the solution flow rate increases, the dry areas shrink in size, thereby increasing the dehumidification rate as indicated in Fig. 8. At an air inlet temperature of 27.7°C, air inlet humidity ratio of 19.03 g/kg, solution inlet temperature of 21.4°C, and solution inlet concertation of 33.89% (i.e., a water vapor pressure potential of 2.24 kPa), Xiao et al. [31] reported a dehumidification rate of 0.073 g/m^2-s for an advanced internally-cooled membrane-based liquid-desiccant dehumidifier. At a water vapor pressure potential of 2.3 kPa and a solution flow rate of 2.8 g/s, the proposed adiabatic textured dehumidifier surface results in a moisture removal rate of 0.1 g/m^2-s, a 37% improvement compared with that of Xiao et al. [31] employing an internally-cooled membrane-based liquid-desiccant dehumidifier.

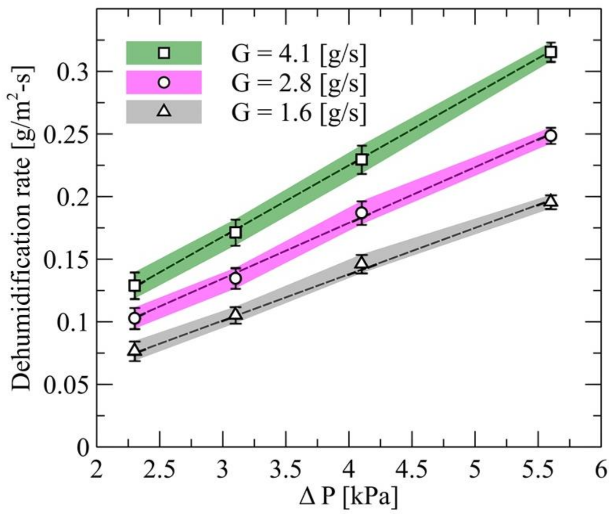

Fig. 8: Dehumidification rate of the 2nd gen. texture design as a function of water vapor pressure potential at different solution flow rates.

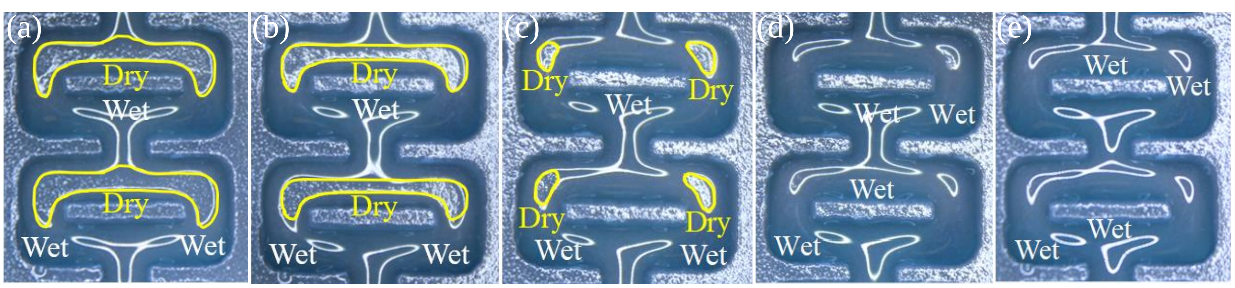

Fig. 9: Interfacial flow distribution patterns of the 2nd gen. texture design at different solution flow rates of (a) 1.6, (b) 2.8, (c) 4.1, (d) 5.4, and (e) 6.5 g/s. The texture length scale is 3 mm.

Fig. 10 shows the dehumidification rate of the textured surface with the partitioned offset-strip fins as a function of LiBr solution flow rate at a fixed water vapor pressure potential of 4.1 kPa. As evident, the dehumidification rate shows two different behaviors to the LiBr solution flow rate. At low LiBr flow rates (i.e., 1.6 to 5.4 g/s), the dehumidification rate increase with the solution flow rate. This is because the effective desiccant-air interfacial area available for the dehumidification process increases with the solution flow rate, consistent with the flow distribution patterns shown in Fig. 9. At high LiBr solution flow rates (i.e., 7 to 9 g/s), the dehumidification rate reaches a plateau with no sensitivity to the solution flow rate. This is attributed to the effective desiccant-air area available for the dehumidification process, which remains constant at high solution flow rates. Therefore, the dehumidification rate becomes independent of the solution flow rate.

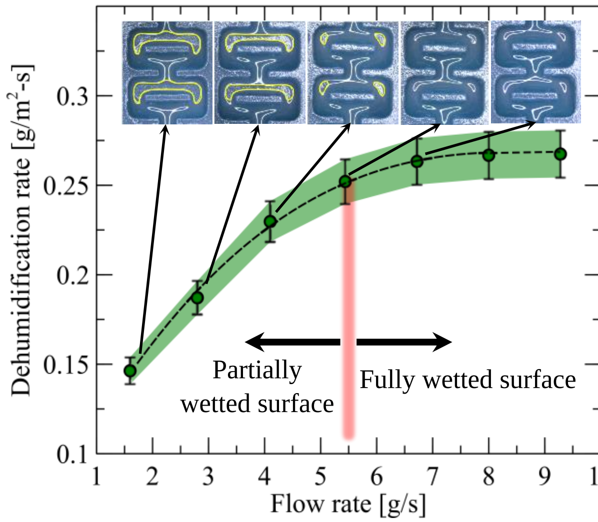

Fig. 10: Dehumidification rate of the 2nd gen. texture design as a function of LiBr solution flow rate. The inserted images show the corresponding solution flow

4.4. System thermal efficiency

Fig. 11 shows variations of the system thermal efficiency of the two textured surfaces as a function of LiBr solution flow rate at a fixed water vapor pressure potential of 5.6 kPa and air volumetric flow rate of 34 m^3/h. As shown, the overall system thermal efficiencies of both textured surfaces decrease with the solution flow rate. The system thermal efficiency is directly proportional to the dehumidification rate and inversely proportional to the thermal energy required for the desorption process. At higher solution flow rates, both the dehumidification rate and desorption thermal energy increase. However, at higher solution flow rates, the rise in the thermal energy required for the desorption process is more than the rise in the dehumidification rate, thereby decreasing the overall thermal efficiency. Additionally, at a fixed solution flow rate, the partitioned offset-strip fins offer a higher system thermal efficiency compared with the drop-shaped structures. For instance, at a LiBr solution flow rate of 4.1 g/s, the partitioned offset-strip fins show a system thermal efficiency of 67.5%, which is 11% higher than that of the drop-shaped structures. This is attributed to the dehumidification rate of the 2nd generation texture design, which is higher than that of the 1st generation design at a given LiBr solution flow rate. Although the desorption thermal energy of the 2nd generation design is slightly higher than that of the 1st generation design due to a higher dehumidification rate, the effect of the dehumidification rate on the overall thermal efficiency dominates. This subsequently increases the overall thermal efficiency of the partitioned offset-strip fins at a given solution flow rate. At a dehumidification capacity of 1.05 kg/h and an input regeneration energy of 1252 W, Xiao et al. [31] reported a thermal energy efficiency 0.49 for an advanced internally-cooled membrane-based liquid-desiccant dehumidifier. At a solution flow rate of 2.8 g/s, the system thermal efficiency of the proposed system is 0.75, a 53% improvement compared with that of Xiao et al. [31] employing a membrane-based liquid-desiccant dehumidifier.

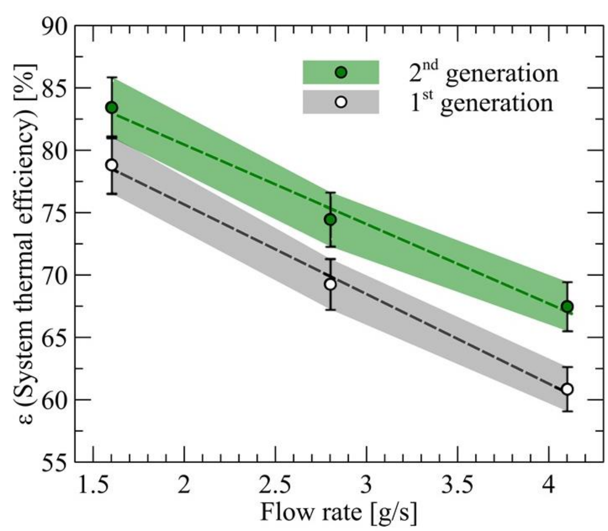

Fig. 11: System efficiency of the two textured surfaces as a function of LiBr solution flow rate.

5. Conclusions

A custom-made well-equipped dehumidification test setup was employed to examine the role of surface textures in moisture removal rate and energy efficiency of liquid-desiccant-based air dehumidifier systems. The dehumidification performance of two textured surfaces with the drop-shaped structures and partitioned offset-strip fins were studied to understand the complex dependency between surface topology, interfacial flow physics, and dehumidification performance. The flow visualization patterns showed that there is an intermediate texture density minimizing the solid-air dry area while maximizing the desiccant-air interfacial area.

The experimental results showed that the dehumidification rate of both textured surfaces increases with the water vapor pressure potential for all air and solution flow conditions examined. The textured surface employing the partitioned offset-strip fins demonstrated a higher dehumidification rate than the textured surface with the drop-shaped structures. For instance, the moisture removal rate of the partitioned offset-strip fins is 33% higher than that of the drop-shaped structures at a LiBr solution flow rate of 4.1 g/s and a partial water vapor potential of 5.6 kPa. Additionally, the results showed that the dehumidification rate of the textured surfaces initially increases with the LiBr solution flow rate as the desiccant-air interfacial area increases. At high LiBr solution flow rates, the dehumidification rate is insensitive to the solution flow rate as the surface gets fully wetted. At a water vapor pressure potential of 2.3 kPa and a solution flow rate of 2.8 g/s, experimental results indicated a moisture removal rate of 0.1 g/m^2-s for the proposed partitioned offset-strip fins, a 37% improvement compared with that of advanced internally-cooled membrane-based liquid-desiccant dehumidifiers. Furthermore, the textured surface with the partitioned offset-strip fins demonstrated a higher overall system thermal efficiency compared with the textured surface employing drop-shaped structures. For instance, the overall system efficiency of the portioned offset-strip fins is 11% higher than that of the drop-shaped structures at a LiBr solution flow rate of 4.1 g/s. A high moisture removal rate of the textured surface with the partitioned offset-strip fins at a low desiccant flow rate led to an overall system thermal efficiency of 0.75, a 53% enhancement compared with the membrane-based liquid-desiccant dehumidifiers. In summary, the present study revealed that surface textures of a dehumidifier module not only affect the moisture removal rate (i.e., the capital cost of a dehumidifier system) but also the overall system energy efficiency (i.e., the operating cost of a dehumidifier system).

Acknowledgments

This study was sponsored by the US Department of Energy's Office of Energy Efficiency and Renewable Energy (EERE) under the Building Technology Office Award Number DEEE0008685. The authors would like to acknowledge Mr. Antonio Bouza and Mr. Mohammed Khan, Technology Managers, and Mr. Andrew Kobusch, Project Engineer, HVAC, Water Heating, and Appliance subprogram, Building Technologies Office, US Department of Energy.

References

[1] The Future of Cooling - Opportunities for energy-efficient air conditioning. International Energy Agency; 2018. https://doi.org/10.1787/9789264301993-en.

[2] Peña X, Alonso L, Diaz de Mendibil A, Prieto J, Gommed K. Hybrid liquid desiccant system

design and operation under high latent load conditions in Taiwan. Int J Refrig 2019;105:41–9. https://doi.org/10.1016/j.ijrefrig.2018.11.011.

[3] Gurubalan A, Maiya MP, Geoghegan PJ. A comprehensive review of liquid desiccant air conditioning system. Appl Energy 2019;254:113673. https://doi.org/10.1016/j.apenergy.2019.113673.

[4] Dong C, Hibiki T, Zhang L, Lu L. Falling film liquid desiccant air dehumidification. Exp Comput Multiph Flow 2020;2:187–98. https://doi.org/10.1007/s42757-019-0036-8.

[5] Moon CG, Bansal PK, Jain S. New mass transfer performance data of a cross-flow liquid desiccant dehumidification system. Int J Refrig 2009;32:524–33. https://doi.org/10.1016/j.ijrefrig.2008.06.011.

[6] Zhang L, Hihara E, Matsuoka F, Dang C. Experimental analysis of mass transfer in adiabatic structured packing dehumidifier/regenerator with liquid desiccant. Int J Heat Mass Transf 2010;53:2856–63. https://doi.org/10.1016/j.ijheatmasstransfer.2010.02.012.

[7] Kumar R, Asati AK. Experimental Study on Effectiveness of Celdek Packed Liquid Desiccant Cooling System. Heat Transf Eng 2018;39:914–22. https://doi.org/10.1080/01457632.2017.1338869.

[8] Liu XH, Zhang Y, Qu KY, Jiang Y. Experimental study on mass transfer performances of cross flow dehumidifier using liquid desiccant. Energy Convers Manag 2006;47:2682–92. https://doi.org/10.1016/j.enconman.2005.10.035.

[9] Salins SS, Reddy SVK, Kumar S. Assessment of process parameters in a dehumidification process using biomass-based wood shaving as a packing material. Indoor Built Environ 2021;0:1–14. https://doi.org/10.1177/1420326X211008509.

[10] Longo GA, Gasparella A. Experimental analysis on chemical dehumidification of air by liquid desiccant and desiccant regeneration in a packed tower. J Sol Energy Eng Trans ASME 2004;126:587–91. https://doi.org/10.1115/1.1637642.

[11] Mansuriya K, Raja BD, Patel VK. Experimental assessment of a small scale hybrid liquid desiccant dehumidification incorporated vapor compression refrigeration system: An energy saving approach. Appl Therm Eng 2020;174:115288. https://doi.org/10.1016/j.applthermaleng.2020.115288.

[12] Gao WZ, Liu JH, Cheng YP, Zhang XL. Experimental investigation on the heat and mass transfer between air and liquid desiccant in a cross-flow dehumidifier. Renew Energy 2012;37:117–23. https://doi.org/10.1016/j.renene.2011.06.006.

[13] Mandow W, Mützel M, Fleig D, Jordan U, Vajen K, Lowenstein A. Comparison of Modeled and Measured Heat and Mass Transfer in a Liquid Desiccant Air-Conditioning System, 2019, p. 1–11. https://doi.org/10.18086/eurosun2018.04.10.

[14] Naik BK, Muthukumar P. Experimental investigation and parametric studies on structured packing chamber based liquid desiccant dehumidification and regeneration systems. Build Environ 2019;149:330–48. https://doi.org/10.1016/j.buildenv.2018.12.028.

[15] Cho HJ, Cheon SY, Jeong JW. Experimental analysis of dehumidification performance of counter and cross-flow liquid desiccant dehumidifiers. Appl Therm Eng 2019;150:210–23. https://doi.org/10.1016/j.applthermaleng.2019.01.006.

[16] Qi R, Dong C, Zhang LZ. A review of liquid desiccant air dehumidification: From system to material manipulations. Energy Build 2020;215:109897. https://doi.org/10.1016/j.enbuild.2020.109897.

[17] Monnier H, Mhiri N, Falk L. Falling liquid film stability in microgas/liquid absorption. Chem Eng Process Process Intensif 2010;49:953–7. https://doi.org/10.1016/j.cep.2010.05.001.

[18] Das RS, Jain S. Experimental investigations on a solar assisted liquid desiccant cooling system with indirect contact dehumidifier. Sol Energy 2017;153:289–300. https://doi.org/10.1016/j.solener.2017.05.071.

[19] Mortazavi M, Nasr Isfahani R, Bigham S, Moghaddam S. Absorption characteristics of falling film LiBr (lithium bromide) solution over a finned structure. Energy 2015;87:270–8. https://doi.org/10.1016/j.energy.2015.04.074.

[20] Kang YT, Kim J-K, Park CW. The effect of micro- surface treatment on heat and mass transfer performance for falling film absorption process. Int. Heat Transf. Conf. 12, Begell House; 2019. https://doi.org/10.1615/ihtc12.730.

[21] Park CW, Cho HC, Kang YT. The effect of heat transfer additive and surface roughness of micro-scale hatched tubes on absorption performance. Int. J. Refrig., vol. 27, 2004, p. 264–70. https://doi.org/10.1016/j.ijrefrig.2003.09.008.

[22] Zhi J, Dong C, Guo M, Qi R, Zhang L zhi. Wettability and performance enhancement with durable super-hydrophilic surfaces for plastic liquid desiccant dehumidification systems. Energy Build 2019;187:77–85. https://doi.org/10.1016/j.enbuild.2019.01.041.

[23] Prieto J, Ortiga J, Coronas A. Experimental performance of polymeric air-solution contactors for liquid desiccant systems. Appl Therm Eng 2017;121:576–84. https://doi.org/10.1016/j.applthermaleng.2017.04.100.

[24] Dong C, Qi R, Zhang L, Lu L. Performance enhancement of solar-assisted liquid desiccant dehumidifiers using super-hydrophilic surface. Energy Build 2019;199:461–71. https://doi.org/10.1016/j.enbuild.2019.07.027.

[25] Wen T, Lu L, Dong C. Enhancing the dehumidification performance of LiCl solution with surfactant PVP-K30. Energy Build 2018;171:183–95. https://doi.org/10.1016/j.enbuild.2018.04.031.

[26] Fu Lin SJ, Shigang Z. Experimental study on vertical vapor absorption into LiBr solution with and without additive. Appl Therm Eng 2011;31:2850–4. https://doi.org/10.1016/j.applthermaleng.2011.05.010.

[27] Yang L, Du K, Niu XF, Cheng B, Jiang YF. Experimental study on enhancement of ammonia-water falling film absorption by adding nano-particles. Int J Refrig 2011;34:640–7. https://doi.org/10.1016/j.ijrefrig.2010.12.017.

[28] Ali A, Vafai K, Khaled ARA. Analysis of heat and mass transfer between air and falling film in a cross flow configuration. Int J Heat Mass Transf 2004;47:743–55. https://doi.org/10.1016/j.ijheatmasstransfer.2003.07.017.

[29] Kang YT, Kim HJ, Lee K Il. Heat and mass transfer enhancement of binary nanofluids for H2O/LiBr falling film absorption process. Int J Refrig 2008;31:850–6. https://doi.org/10.1016/j.ijrefrig.2007.10.008.

[30] Gurubalan A, Maiya MP, Tiwari S. Performance characterization of a novel membrane-based liquid desiccant air conditioning system. Int J Refrig 2020;120:445–59. https://doi.org/10.1016/j.ijrefrig.2020.09.007.

[31] Xiao L, Yang M, Yuan WZ, Huang SM. Performance characteristics of a novel internally-cooled plate membrane liquid desiccant air dehumidification system. Appl Therm Eng 2020;172:115193. https://doi.org/10.1016/j.applthermaleng.2020.115193.

[32] Chen Z, Zhu J, Bai H, Yan Y, Zhang L. Experimental study of a membrane-based dehumidification cooling system. Appl Therm Eng 2017;115:1315–21. https://doi.org/10.1016/j.applthermaleng.2016.10.153.

[33] Bui TD, Chen F, Nida A, Chua KJ, Ng KC. Experimental and modeling analysis of membrane-based air dehumidification. Sep Purif Technol 2015;144:114–22. https://doi.org/10.1016/j.seppur.2015.02.019.

[34] Bergero S, Chiari A. Performance analysis of a liquid desiccant and membrane contactor hybrid air-conditioning system. Energy Build 2010;42:1976–86. https://doi.org/10.1016/j.enbuild.2010.06.003.

[35] Isetti C, Nannei E, Orlandini B. Three-fluid membrane contactors for improving the energy efficiency of refrigeration and air-handling systems. Int J Ambient Energy 2013;34:181–94. https://doi.org/10.1080/01430750.2012.755905.

[36] Qu M, Abdelaziz O, Gao Z, Yin H. Isothermal membrane-based air dehumidification: A comprehensive review. Renew Sustain Energy Rev 2018;82:4060–9. https://doi.org/10.1016/j.rser.2017.10.067.

[37] Woods J, Kozubal E. A desiccant-enhanced evaporative air conditioner: Numerical model and experiments. Energy Convers Manag 2013;65:208–20. https://doi.org/10.1016/j.enconman.2012.08.007.

[38] Gurubalan A, Maiya MP, Tiwari S. Experiments on a novel membrane-based liquid desiccant dehumidifier for hybrid air conditioner. Int J Refrig 2019;108:271–82. https://doi.org/10.1016/j.ijrefrig.2019.09.004.

[39] Xing R, Rao Y, TeGrotenhuis W, Canfield N, Zheng F, Winiarski DW, et al. Advanced thin zeolite/metal flat sheet membrane for energy efficient air dehumidification and conditioning. Chem Eng Sci 2013;104:596–609. https://doi.org/10.1016/j.ces.2013.08.061.

[40] Miller WA, Perez-Blanco H. Vertical-tube aqueous LiBr falling film absorption using advanced surfaces. Proc Int Absorpt Heat Pump Conf 1994:185–202.

[41] Raisul Islam M, Wijeysundera N., Ho J. Performance study of a falling-film absorber with a film-inverting configuration. Int J Refrig 2003;26:909–17. https://doi.org/10.1016/S0140-7007(03)00078-1.

[42] Cui XY, Shi JZ, Tan C, Xu ZP. Investigation of plate falling film absorber with film-inverting configuration. J Heat Transfer 2009;131:1–9. https://doi.org/10.1115/1.3089550.

[43] Luo Y, Shao S, Xu H, Tian C, Yang H. Experimental and theoretical research of a fin-tube type internally-cooled liquid desiccant dehumidifier. Appl Energy 2014;133:127–34. https://doi.org/10.1016/j.apenergy.2014.07.085.

[44] Qi R, Zhi J, Zhang LZ. Wetting improvement of plastic working plate for liquid desiccant

dehumidification systems. Energy Procedia 2019;158:3076–81. https://doi.org/10.1016/j.egypro.2019.01.994.

[45] Liu J, Zhang T, Liu X, Jiang J. Experimental analysis of an internally-cooled/heated liquid desiccant dehumidifier/regenerator made of thermally conductive plastic. Energy Build 2015;99:75–86. https://doi.org/10.1016/j.enbuild.2015.04.023.

[46] Lee JH, Jung CW, Chang YS, Chung JT, Kang YT. Nu and Sh correlations for LiCl solution and moist air in plate type dehumidifier. Int J Heat Mass Transf 2016;100:433–44. https://doi.org/10.1016/j.ijheatmasstransfer.2016.04.100.